Clinical and Experimental Medicine (2026) 26:117
https://doi.org/10.1007/s10238-025-02034-x

RESEARCH

Exploring the correlation between ferroptosis-associated biomarkers and MRI-derived parameters in liver fibrosis associated with metabolic dysfunction-associated steatotic liver disease

Meihua Yang[1] · Qian Xu[1] · Fangyan Li[2] · Chen Chen[1] · Tianyuan Wang[1] · Maowen Tang[2] · Menghua Yang[2] · Jian He[2] · Yue Pan[2] · Rao Dai[2] · Pinggui Lei[1,2] · Peng Luo[1,3]

Received: 17 November 2025 / Accepted: 28 December 2025

Abstract

The global prevalence of metabolic dysfunction-associated steatotic liver disease (MASLD) continues to rise, and the accurate, non-invasive assessment of liver fibrosis remains an important clinical challenge. This study aimed to identify ferroptosis biomarkers associated with MASLD-related liver fibrosis progression, explore their potential biological links with MRI-derived parameters, and provide new clues for developing non-invasive diagnostic strategies for ferroptosis. A MASLD-related liver fibrosis model was established using 30 Sprague-Dawley (SD) rats. Hub differentially expressed ferroptosis-related genes (DE-FRGs) were identified through the integration of weighted gene co-expression network analysis (WGCNA), differential expression analysis, and LASSO regression. The role of ferroptosis in MASLD was evaluated using transmission electron microscopy (TEM) and measurements of glutathione (GSH) and Fe^{2+} content. T2*, R2*, and proton density fat fraction (PDFF) were obtained through magnetic resonance imaging (MRI) and were analyzed for correlations with hub DE-FRGs and Fe^{2+} levels. A total of eight hub DE-FRGs were identified: *Pck2*, *Idh2*, *Nr1d1*, *Fads1*, *Sat1*, *Abhd12*, *Got1*, and *Srebf1*. Enrichment analyses revealed that these hub DE-FRGs were predominantly implicated in carbohydrate response, amino acid biosynthesis, insulin resistance, and the AMPK signaling pathway. TEM and biochemical markers analyses demonstrated an association between MASLD-related liver fibrosis and ferroptosis. MRI-derived parameters were significantly correlated with Fe^{2+} levels and the expression of hub DE-FRGs. This study preliminarily identified hub DE-FRGs associated with liver fibrosis in MASLD and their signaling pathways, verified indirect indicators related to ferroptosis, and proposed their potential correlation with MRI-derived parameters.

Keywords Transcriptome sequencing · Ferroptosis · Metabolic dysfunction-associated steatotic liver disease · Liver fibrosis · MRI-derived parameters

Abbreviations

MASLD	Metabolic dysfunction-associated steatotic liver disease
FRGs	Ferroptosis-related genes
MRI	Magnetic resonance imaging
PDFF	Proton-density fat fraction
HFHC	High-fat, high-cholesterol
HE	Hematoxylin-eosin
PCA	Principal-component analysis
DEGs	Differentially expressed genes
GO	Gene Ontology
KEGG	Kyoto Encyclopedia of Genes and Genomes
MF	Molecular Function
CC	Cellular Component
BP	Biological Process
WGCNA	Weighted Gene Co-expression Network Analysis
DE-FRGs	Differentially expressed ferroptosis-related

Meihua Yang M.D., Qian Xu M.D. and Fangyan Li M.D. contributed equally to this work.

Extended author information available on the last page of the article

Published online: 21 January 2026

	genes
GSH	Glutathione
TEM	Transmission electron microscopy
GS	Gene significance
MM	Module membership
PUFAs	Polyunsaturated fatty acids
HCC	Hepatocellular carcinoma

Introduction

Metabolic dysfunction-associated steatotic liver disease (MASLD) is a chronic hepatic fat accumulation disorder caused by non-alcoholic factors. It is characterized by hepatocellular steatosis and steatohepatitis. As the disease progresses, liver fibrosis and cirrhosis may develop, and in some cases, it can advance to hepatocellular carcinoma (HCC) [1]. Studies have indicated that MASLD is linked to metabolic syndrome and may increase the risk and progression of atherosclerosis, cardiovascular disease, and diabetes [2]. According to the recent epidemiological data, the global prevalence of MASLD has reached approximately 30% [3, 4].

Liver fibrosis is a pivotal determinant of MASLD progression and prognosis. Although liver biopsy remains the gold standard for confirming fibrosis, its invasiveness, which entails risks of bleeding, infection, and other complications limits its widespread clinical use [5]. Therefore, the development of non-invasive, accurate, and reproducible assessment tools has become a major focus of current research. Rapid advances in genomic technologies have greatly enhanced our understanding of the molecular mechanisms underlying MASLD-related liver fibrosis [6]. As a key branch of genomics, transcriptomics shows great promise for evaluating liver fibrosis in the context of this disease [7]. Ferroptosis, a distinct form of cell death identified in recent years, is particularly noteworthy [8]. The liver, as the primary reservoir of lipids and iron, plays a pivotal role in the progression of liver diseases such as MASLD. Studies have shown that acetaminophen overdose-induced acute liver injury is accompanied by ferroptosis in the liver [9]. Research by Shinya Tsurusaki et al. indicated that ferroptosis could be a potential trigger for steatohepatitis [10]. Therefore, identifying ferroptosis-related genes (FRGs) associated with MASLD-related liver fibrosis has potential significance for advancing our understanding of the disease, which may help in clinical diagnosis and provide prospects for early therapeutic intervention.

In recent years, advances in imaging technology and transcriptomics have provided new perspectives for diagnosing and mechanistically exploring MASLD-related liver fibrosis. Radiobioinformatics integrates quantitative imaging with bioinformatics to identify alterations in potential signaling pathways or biomarkers [11]. Currently, non-invasive imaging techniques have been widely used in this field to explore disease-related genomes and gene mutations, and they have been extensively applied in research on oncology, cardiovascular diseases, neurodegenerative disorders [12], and HCC [13]. Magnetic resonance imaging (MRI), as a non-invasive imaging tool, holds great potential for quantifying hepatic fat deposition and fibrosis [14]. Its derived parameters T2*, R2* and proton-density fat fraction (PDFF) can precisely measure pathophysiological alterations in liver tissue, providing objective evidence for the non-invasive assessment of liver fibrosis [15]. Nevertheless, radiogenomic studies specifically focused on MASLD-related fibrosis remain scarce, leaving considerable room for further exploration.

This study aims to address the current lack of bioinformatics research on FRGs in MASLD-related fibrosis and the absence of integrated analysis with MRI-derived parameters. We established an animal model of MASLD-related fibrosis, used transcriptome sequencing data to identify FRGs and signaling pathways associated with fibrosis progression, and validated indirect indicators related to ferroptosis. Furthermore, the correlation between these indicators and MRI-derived parameters was analyzed to explore their biological connections. This study is expected to provide potential ferroptosis biomarkers for the progression of MASLD-related liver fibrosis and offer new theoretical foundations and practical guidance for developing non-invasive diagnostic methods for ferroptosis.

Materials and methods

Establishment of animal models

A total of 30 Sprague-Dawley (SD) rats were enrolled and randomly assigned to either a model group (n = 20) or a control group (n = 10). The control group was fed standard diet and water, while the model group was fed a high-fat, high-cholesterol (HFHC) diet and drinking water containing 23.1 g/L fructoseglucose syrup. The model group was further randomized into two subgroups (n = 10) according to the 8-week and 12-week time points. The 12-week subgroup received intraperitoneal injections of CCl_4 (diluted 1:3 v/v in olive oil) at 0.5 mL/kg twice weekly for 4 weeks, starting at week 8 [16]. All animal-related protocols were approved by the Guizhou Medical University Ethical Committee (approval No. 2304182). The overall study design is shown in figure 1.

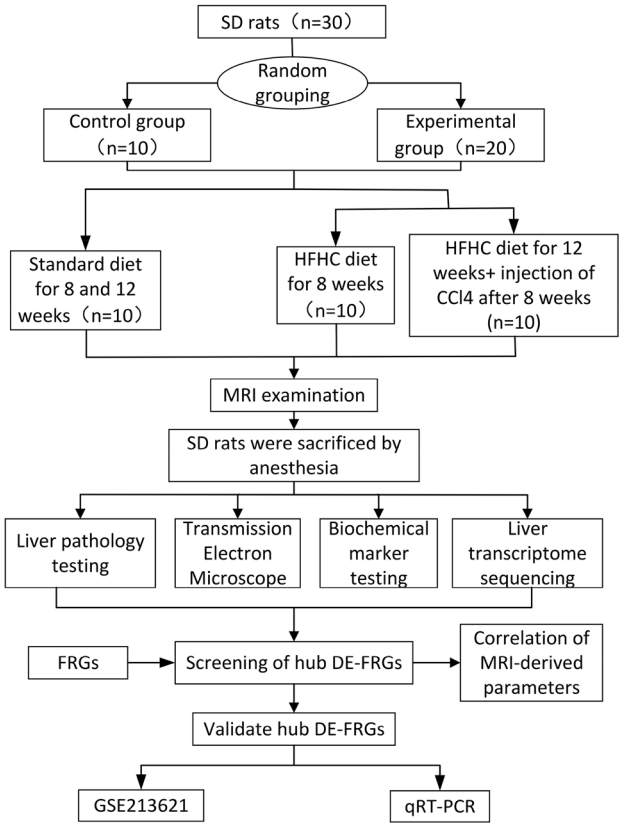

Fig. 1 Flowchart of the study design for the MASLD liver fibrosis rat model

MRI examination and measurement

After the rat was secured in the animal holder, tribromoethanol was administered intraperitoneally via the right lower quadrant for anesthesia. Following anesthesia induction, MRI examination was conducted using a four-channel animal RF coil (Magtron Inc., Jiangyin, China; model WK602). The abdominal scanning area was fully exposed. The upper abdomen was then gently wrapped with padding to minimize respiratory motion artifacts. A sagittal localizer scan was obtained to identify the optimal imaging plane centered on the liver. The MRI protocol included standard IDEAL-IQ, T2WI, and T2* mapping. All images were retrospectively and blindly reviewed by an experienced radiologist blinded to group allocation using an ADW 4.7 workstation (GE Healthcare, USA). For quantitative analysis, regions of interest (ROIs) were selected from IDEAL-IQ and T2* mapping, carefully avoiding large intrahepatic vessels, bile ducts, the gallbladder, abdominal adipose tissue, and areas affected by intrapulmonary air. Three ROIs (approximately 8 mm^2 each) were taken from per layer. The mean values of T2*, R2*, and PDFF were calculated and recorded numerically, and the corresponding images were saved.

Liver histopathological examination

Immediately after the MRI examination, fresh liver tissue was obtained from each rat, one 1.0-cm^3 cube was taken from both the left and right lobes and immersed in 4% neutral-buffered formalin. After complete fixation, the sections were subsequently stained with Prussian blue, hematoxylin-eosin (HE), and Massons trichrome. One experienced pathologist, blinded to all group assignments and imaging data, independently evaluated the slides, and graded fibrosis using the METAVIR system. According to this system, F0 represents no fibrosis (the control group), F1-F4 represent the fibrosis group, where F1 and F2 represent the non-advanced fibrosis group, and F3 and F4 represent the advanced fibrosis group.

Data set collection

Total RNA was extracted from liver tissue using TRIzol reagent. Purity and concentration were measured with a NanoDrop 2000 spectrophotometer (Thermo Scientific, USA), and RNA integrity was verified using an Agilent 2100 Bioanalyzer (Agilent Technologies, Santa Clara, CA, USA). Libraries were prepared with the VAHTS Universal V10 RNA-seq Library Prep Kit (Premixed Version) according to the manufacturers instructions and then sequenced on an Illumina NovaSeq 6000 platform. These procedures were performed by Shanghai OE Biotech Co., Ltd. Additionally, the GSE213621 dataset, which includes mRNA-seq data from 69 control samples and 299 MASLD samples, was downloaded from the GEO repository (https://www.ncbi.nlm.nih.gov/geo/), and 564 FRGs were retrieved from the FerrDb database (http://www.zhounan.org/ferrdb/current/).

Screening of DEGs

First, a sample-to-sample correlation heatmap was generated from the expression matrix to assess overall reproducibility. Then, principal component analysis (PCA) was performed to visualize within-group clustering and between-group separation among subgroups. Using the R limma package to calculate the differential expression between the control group and each fibrosis group (non-advanced fibrosis group, advanced fibrosis group, and fibrosis group), retain genes with $|\log_2 \text{fold change}| > 1$ and adjusted p value < 0.05 as differentially expressed genes (DEGs). Volcano plots were generated with ggplot2, hierarchical clustering heatmaps with pheatmap, and Venn diagrams were constructed to identify DEGs common to all three contrasts as genes associated with MASLD fibrosis progression.

GO and KEGG enrichment analyses

The DEGs were subjected to Gene Ontology (GO) and Kyoto Encyclopedia of Genes and Genomes (KEGG) enrichment analyses. GO covers three domains: Molecular Function (MF), Cellular Component (CC) and Biological Process (BP). KEGG is a widely used database for investigating diseases, chemicals, drugs, biological processes and genomes. Adjusted p-value < 0.05 is considered statistically significant.

Weighted gene co-expression network analysis (WGCNA)

To identify gene modules with coherent expression patterns and explore their relationship to clinical phenotypes, we constructed a co-expression network from the RNA-seq data using WGCNA and extracted modules whose expression was significantly correlated with hepatic fibrosis ($|r| > 0.6$, $p < 0.05$) for downstream analysis.

Identification and expression levels of hub DE-FRGs

Intersect DEGs and WGCNA results with the 564 known FRGs, and designate the overlapping genes as differentially expressed ferroptosis-related genes (DE-FRGs). A LASSO model was then constructed using the R package glmnet to identify hub DE-FRGs. To clearly illustrate the entire screening process, we mapped out the process of screening hub DE-FRGs (Online Resource 1). These hub DE-FRGs subsequently analyzed through GO and KEGG enrichment analyses, and their expression levels across the control, non-advanced fibrosis, and advanced fibrosis groups were visualized using box-dot plots generated with the ggpubr package.

Table 1 List of the qRT-PCR primers used in this study

Gene	Forward primer	Reverse primer
β-actin	TGCTATGTTGCCCTAGACTTCG	GTTGGCATAGAGGTCTTTACGG
Got1	TCCATCTTTGTCCTCCACGC	GCCCAGGCATCTTTCTCTAGG
Nr1d1	CAAGCTTAACGGCATGGTGC	GCCAACGGAGAGACACTTCT
Idh2	GGAAGAGCCCTAACGGAACTATC	CGAAATGGACTCGTCGGTGT
Fads1	ACTTTGGGCACCTGTCCGT	GTCTTTGCGGAAGCAGTTGG
Pck2	TGCCATGGCTGCTATGTACC	TTTGGATGCTACGGCATGGT
Sat1	AAGCCAGGTTGCTATGAAGTGT	TGAATAGTCTCCATCCCTCTTCACT

Ferroptosis-associated markers

To verify indicators related to ferroptosis, five liver samples from each group were selected for experimental analysis. The liver samples were homogenized in PBS (0.1 g tissue : 0.9 mL buffer) and centrifuged at 10 000 × g for 10–15 min at 4 °C, the resulting supernatant was used for subsequent assays. Glutathione (GSH) and Fe^{2+} levels were determined using commercial kits, with every step and calculation performed exactly as specified by the manufacturer. Additionally, 2 mm^3 fragments were cut from freshly isolated rat liver, immediately fixed overnight in 2.5% glutaraldehyde, after embedding and sectioning, examined by transmission electron microscopy (TEM) for ultrastructural changes.

Validation of hub DE-FRGs

The hub DE-FRGs were further validated using the external dataset GSE213621. Four liver samples from each group were taken for qRT-PCR validation. Total RNA was first extracted using TRIzol reagent, and then it was reverse transcribed into cDNA according to the instructions of the cDNA synthesis kit (G3337, Wuhan Saiweier Biotechnology Co., Ltd.). After preparing the qRT-PCR reaction system, amplification was carried out on a real-time fluorescent quantitative PCR instrument. Three technical replicates were set up for each sample. The relative expression levels of the target genes were calculated using the 2-ΔΔCt method, with the *β-actin* gene used as an internal reference for normalization. Primer sequences are listed in Table 1.

Correlation analysis of hub DE-FRGs, Fe^{2+}, and MRI-derived parameters

Spearman correlation analysis was used to examine the relationships between Fe^{2+} content, the expression levels of hub DE-FRGs, and MRI-derived parameters such as R2*, T2*, and PDFF, offering molecular insights into the observed imaging phenotypes.

Statistical analysis

Differential expression analysis was conducted using R 4.4.2 (https://www.r-project.org). Enrichment analyses, spearman correlation analysis, and Venn diagrams were generated using the Bioinformatics Platform (http://www.bioinformatics.com.cn). Biochemical data and qRT-PCR results were visualized with GraphPad Prism 9.5. WGCNA was performed using OEbiotech Cloud (https://cloud.oebiotech.com), and Sankey plots were created with Genes Cloud (https://www.genescloud.cn/home). In both transcriptome and GO enrichment analyses, multiple test correction was applied.

For GO enrichment analysis, an adjusted p-value < 0.05 was used as the criterion. DEGs were screened using an adjusted p-value < 0.05 and $|\log_2(\text{fold change})| \geq 1$ as criteria. For qRT-PCR and biochemical indicator measurements, the data were first tested for normality, and comparisons among multiple groups were performed using one-way ANOVA, with results presented as mean ± standard deviation (SD). For correlation analysis, based on the data distribution, Spearman correlation analysis was selected. A p-value less than 0.05 was considered statistically significant. ns, indicates the difference is not statistically significant, * $p < 0.05$, ** $p < 0.01$, *** $p < 0.001$.

Results

Liver histopathological and MRI imaging results

Figure 2 presents representative pathological findings and MRI imaging from each rat group. On HE-stained sections, the control group exhibited intact lobular architecture with orderly hepatic cords. In non-advanced fibrosis (F1-F2), the structure was largely preserved, displaying only scattered spotty necrosis. Advanced fibrosis (F3-F4) revealed marked architectural disarray, extensive hepatocellular swelling and ballooning degeneration, together with bile-duct proliferation and dense inflammatory infiltrates around portal tracts (Fig. 2a). Masson staining further confirmed the degree of fibrosis: the control group showed virtually no collagen deposition; non-advanced fibrosis exhibited thin blue-green collagen rims around portal and central veins; and advanced fibrosis displayed extensive blue collagen deposition with the formation of characteristic pseudolobules (Fig. 2b). MRI can be used as a tool to evaluate the liver parenchyma in rat models (Fig. 2c). In conclusion, the above results indicate that the MASLD-related liver fibrosis model has been successfully established.

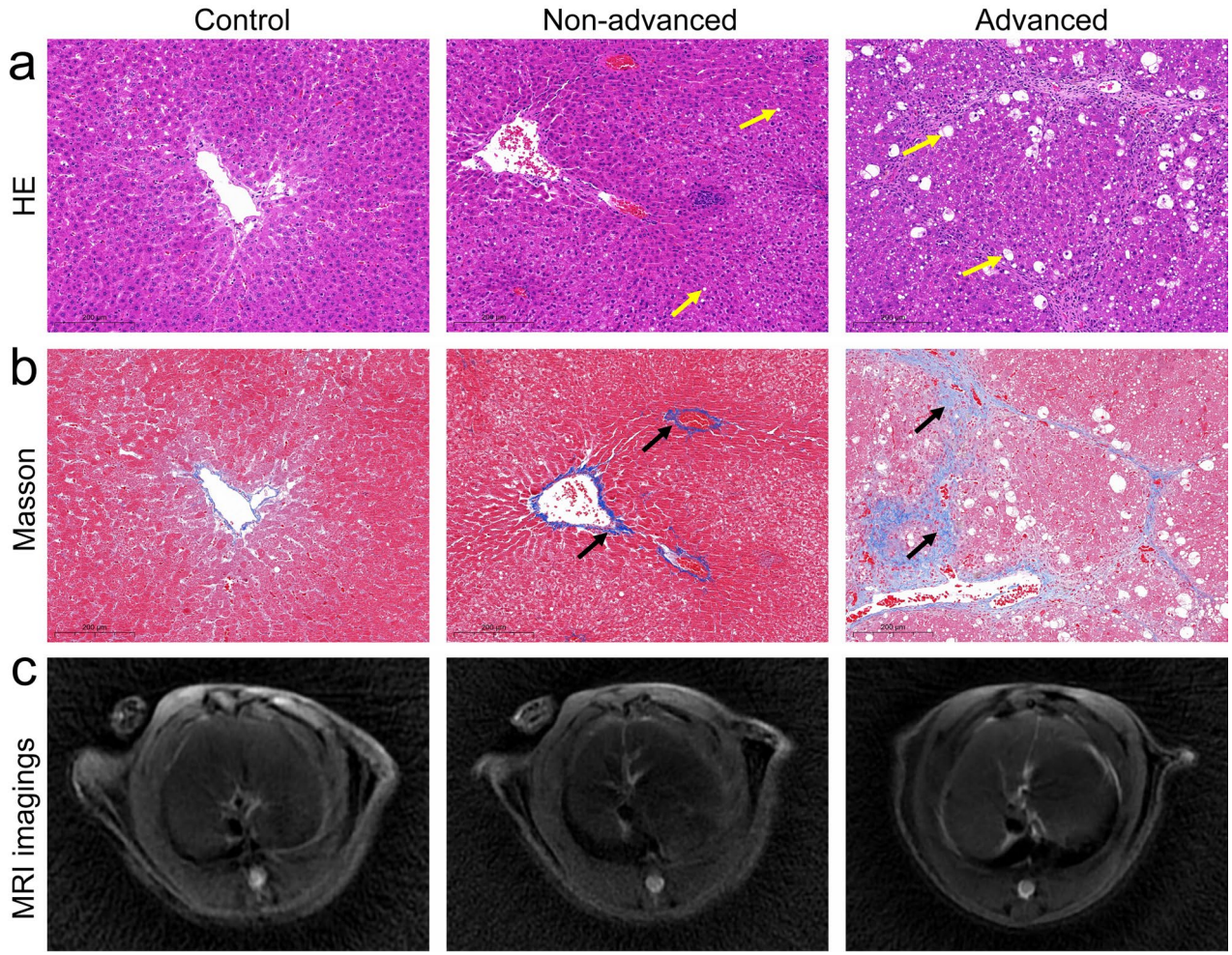

Fig. 2 Pathological results and MRI images of the MASLD liver fibrosis model in rats. **a** HE staining, yellow arrow indicates the fatty degeneration of liver tissue. **b** Masson staining, black arrow indicates blue collagen deposition. **c** Representative MRI images

Identification of DEGs

All samples exhibited high inter-sample correlation with no outliers (Fig. 3a). In the PCA results, samples formed clear boundaries among groups andclustered tightly together within each group (Fig. 3b-d). Differential expression analysis identified 1,204 (control vs. non-advanced fibrosis groups), 3,306 (control vs. advanced fibrosis groups) and 2,488 (control vs. fibrosis groups) DEGs (Fig. 3e), with a total of 1,047 overlapping genes, comprising 865 up-regulated and 182 down-regulated genes (Fig. 3f, Online Table 1).

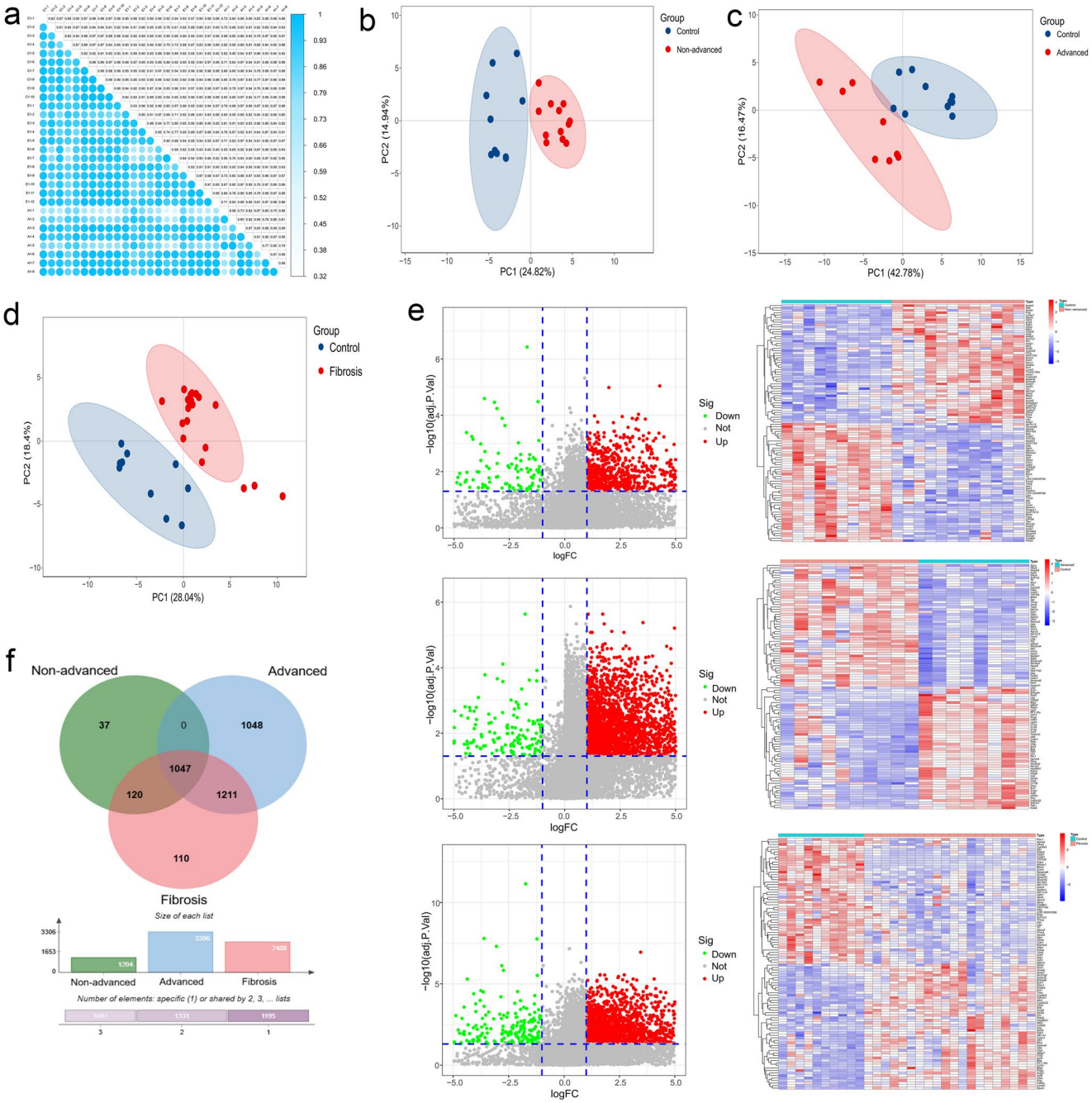

Fig. 3 Identification of DEGs. **a** Heatmap of correlations among 30 samples. **b-d** PCA plot between the control and non-advanced groups (**b**), the control and advanced groups (**c**), and the control and fibrosis groups (**d**). **e** Volcano plot and heatmap display the DEGs between control and non-advanced fibrosis groups, control and advanced fibrosis groups, and control and fibrosis groups, from top to bottom. **f** A total of 1,047 DEGs were identified. Venn diagrams were used to visualize the intersection of three groups of differential expression analysis

DEGs enrichment analysis

GO enrichment analysis revealed that the DEGs were enriched in BP including secondary alcohol metabolic process, alcohol metabolic process, cholesterol metabolic process, cellular lipid catabolic process, sterol metabolic process, and organic acid catabolic process. CC included mitochondrial matrix, cell-substrate junction, lysosome, mitochondrial inner membrane, and peroxisome. MF primarily encompasses oxidoreductase activity, acyltransferase activity, flavin adenine dinucleotide binding, and isomerase activity(Fig. 4a, Online Table 2). KEGG pathway analysis of the DEGs revealed significant enrichment in steroid biosynthesis, fatty acid metabolism, PPAR signaling pathway, nucleotide metabolism, sphingolipid metabolism, and peroxisome-related pathways (Fig. 4b, Online Table 2). Enrichment analysis results suggest that these pathways may be closely related to MASLD-related liver fibrosis.

WGCNA analysis

A scale-free co-expression network was constructed using a soft-thresholding power of $\beta = 8$, which yielded seven gene modules (Fig. 5a-c). Three modules were significantly associated with liver fibrosis: the turquoise module (801 genes) and the yellow module (49 genes) showed positive correlations, while the blue module (201 genes) exhibited a negative correlation (Fig. 5d-f, Online Table 3). We used the genes from these three modules for subsequent analysis.

Screening and expression levels of hub DE-FRGs

The intersection of DEGs, FRGs, and genes from WGCNA modules associated with liver fibrosis identified 20 DE-FRGs (Fig. 6a). LASSO regression analysis of these 20 genes revealed 8 hub DE-FRGs: *Pck2*, *Idh2*, *Nr1d1*, *Fads1*, *Sat1*, *Abhd12*, *Got1*, and *Srebf1* (Fig. 6b-c). *Fads1*, *Got1*, and *Nr1d1* were down-regulated in the liver fibrosis group, whereas *Abhd12*, *Idh2*, *Pck2*, *Sat1*, and *Srebf1* were up-regulated in the liver fibrosis group (Fig. 6d). These 8 genes, which simultaneously meet the criteria of differential expression, WGCNA module membership, and non-zero LASSO coefficients, were identified as hub DE-FRGs for subsequent validation and analysis.

Enrichment analysis of hub DE-FRGs

To explore the potential biological processes jointly involving the eight hub DE-FRGs identified through bioinformatics and machine learning, GO and KEGG enrichment analyses were performed. These analyses aimed to provide preliminary insights into the synergistic mechanisms of these hub DE-FRGs. GO enrichment analysis showed that hub DE-FRGs were significantly enriched in the BP and MF categories (adjusted p-value < 0.05), such as response to carbohydrate, regulation of protein secretion, regulation of insulin secretion, carboxy-lyase activity, and acylglycerol lipase activity, however, no significant enrichment was observed for CC (adjusted p-value > 0.05) (Fig. 7a; Table 2). KEGG enrichment analysis revealed that hub DE-FRGs were significantly enriched in pathways including the citrate cycle, arginine and proline metabolism, biosynthesis

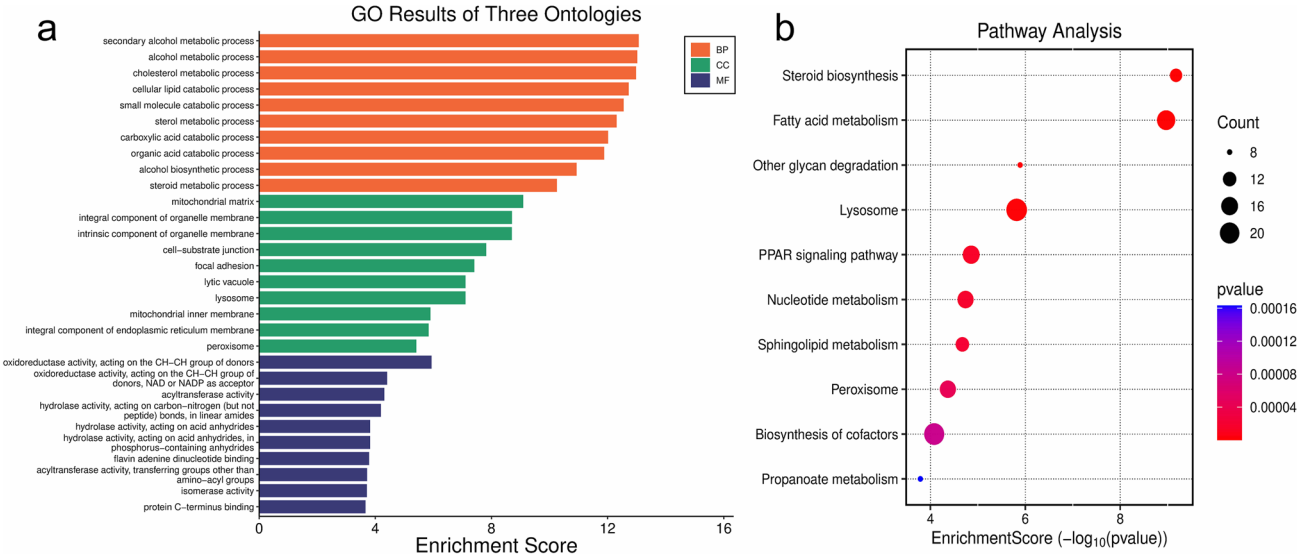

Fig. 4 GO and KEGG enrichment plots of DEGs in MASLD-related liver fibrosis. **a** Bar chart of GO enrichment analysis for DEGs. **b** Bubble chart of KEGG pathway enrichment analysis for DEGs

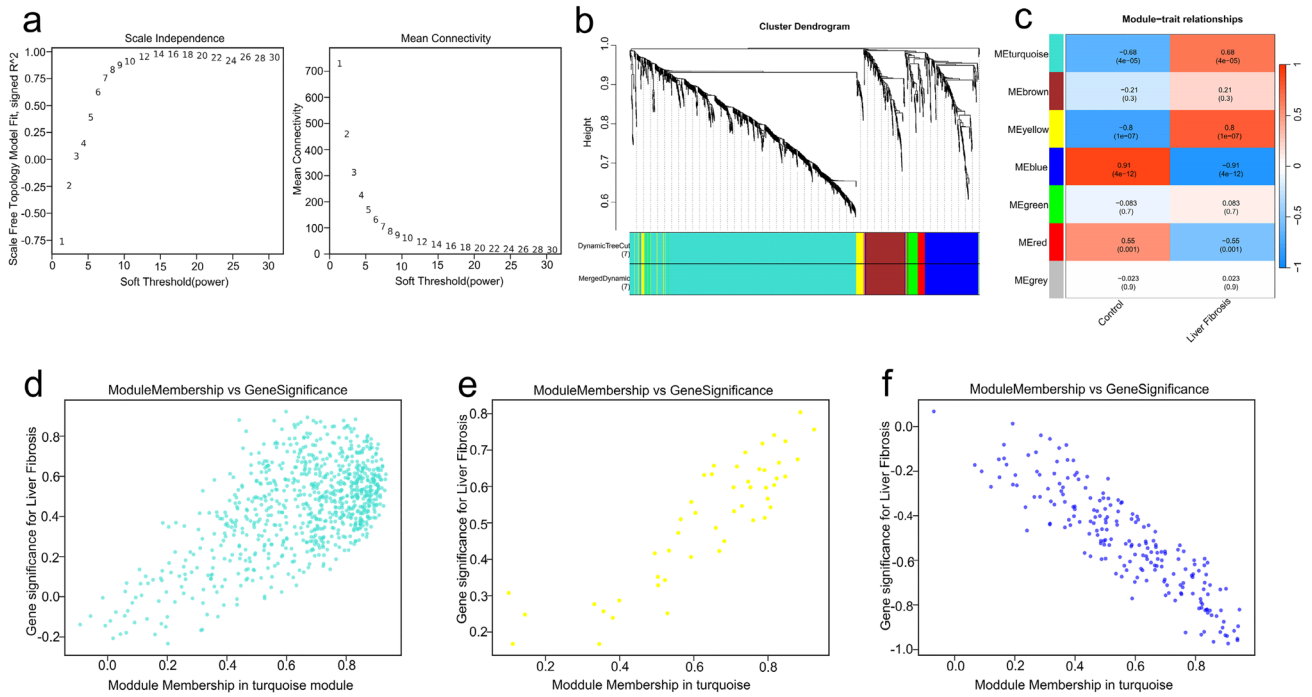

Fig. 5 WGCNA modules in MASLD-related liver fibrosis. **a** Plot of soft-threshold power versus mean connectivity used to determine the optimal soft-thresholding power for network construction. **b** Gene-clustering dendrogram based on topological overlap. **c** Module-trait association heatmap, rows represent modules, and columns represent the corresponding phenotypes, the values in the box represent the correlation coefficient and the significance level (*p*-value), red represents a positive correlation, blue represents a negative correlation, and the depth of the color indicates the strength of the correlation. We selected modules with a correlation greater than 0.6 for analysis. **d-f** Scatter plots of gene significance (GS) vs. module membership (MM) for: the turquoise module (**d**), the yellow module (**e**), and the blue module (**f**)

of amino acids, insulin resistance, and the AMPK signaling pathway (adjusted p-value < 0.05) (Fig. 7b; Table 2).

Indirect indicators related to ferroptosis in rat models

Prussian blue staining revealed scattered deep-blue granules in the livers of rats with non-advanced fibrosis, whereas the advanced fibrosis group exhibited a markedly wider distribution of these iron-positive deposits compared with the control group (Fig. 8a). TEM demonstrated ferroptosis-related ultrastructural alterations in the hepatocyte mitochondria of fibrosis rats, including mitochondrial swelling, increased cristae fragmentation, reduced matrix volume, and a marked decrease in matrix electron density (Fig. 8b). Since GSH reduction and iron accumulation are key mechanisms of ferroptosis, we assessed these parameters. The results showed that, compared with the control group, hepatic GSH activity was significantly decreased in the fibrosis group, and Fe^{2+} levels were elevated in the fibrosis group ($p < 0.05$) (Fig. 8c-d). These findings suggest that ferroptosis may be involved in the progression of MASLD-related liver fibrosis.

Validation of hub DE-FRGs

Analysis of the external dataset GSE213621 revealed that all hub DE-FRGs except *NR1D1* showed statistically significant differential expression between control and fibrosis groups. Among these, *GOT1*, *ABHD12*, and *IDH2* exhibited expression trends consistent with our RNA-seq findings (Fig. 9a). qRT-PCR results demonstrated that *Fads1*, *Got1*, and *Nr1d1* were down-regulated in the fibrosis group, while *Idh2*, *Pck2*, and *Sat1* were up-regulated in the fibrosis group, which aligns with the sequencing analysis results. For the other two hub DE-FRGs, qRT-PCR results showed no statistically significant differences in expression between the control group and the fibrosis group (Fig. 9b).

Correlation analysis of hub DE-FRGs, Fe^{2+}, and MRI-derived parameters

Spearman correlation analysis revealed that PDFF values were significantly associated with all hub DE-FRGs: positively with *Fads1*, *Got1*, and *Nr1d1*, and negatively with *Abhd12*, *Idh2*, *Pck2*, *Sat1*, and *Srebf1* ($p < 0.05$) (Fig. 10a). R2* showed a positive correlation with Fe^{2+}, whereas T2* exhibited a negative correlation with Fe^{2+} ($p < 0.05$) (Fig. 10b). Representative biological functions associated

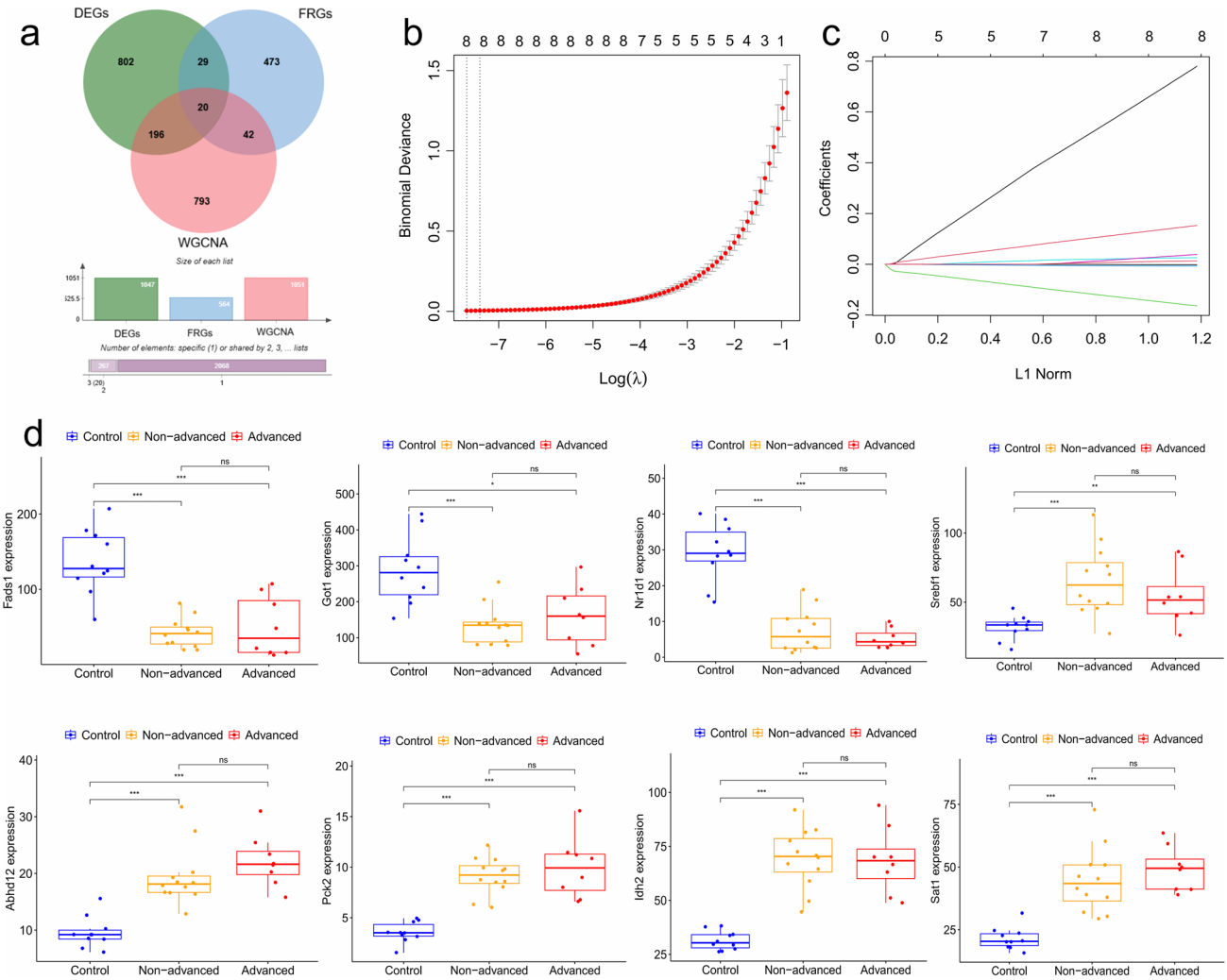

Fig. 6 Screening and expression profiles of hub DE-FRGs. **a** Venn diagram showing the overlap among DEGs, FRGs, and MASLD fibrosis-related module genes identified by WGCNA, obtain 20 DE-FRGs. **b** LASSO regression analysis of 20 DE-FRGs, Y-axis represents the cross-validation curve error, the smaller the value on the vertical axis, the better the fitting performance, the horizontal axis below represents the logarithm of the lambda penalty coefficient, and the horizontal axis above represents the number of variables corresponding to different λ values, the dashed line on the left represents the number of genes corresponding to the minimum error, 8 hub DE-FRGs were selected at the value (lambda.min). **c** LASSO coefficient path diagram, each curve represents the change trajectory of a gene. **d** The boxplot shows the expression levels of the 8 hub DE-FRGs identified by LASSO regression. Results are presented as mean ± standard deviation (SD), statistical analysis was performed using one-way ANOVA. ns, indicates the difference is not statistically significant, * $p<0.05$, ** $p<0.01$, *** $p<0.001$

with these hub DE-FRGs were illustrated in figure. 10c. The correlation results suggest that hub DE-FRGs, Fe^{2+}, and MRI-derived parameters were closely related in MASLD-related liver fibrosis.

Discussion

By integrating bioinformatics and machine learning approaches including differential gene expression analysis, WGCNA, and LASSO regression, we identified eight hub DE-FRGs: *Pck2*, *Idh2*, *Nr1d1*, *Fads1*, *Sat1*, *Abhd12*, *Got1*, and *Srebf1*. Except for *NR1D1*, all other hub DE-FRGs were validated in the GSE213621 dataset, the expression trends of *GOT1*, *ABHD12*, and *IDH2* matched the sequencing results. Furthermore, *Fads1*, *Nr1d1*, *Got1*, *Idh2*, *Pck2*, and *Sat1* were further confirmed by qRT-PCR in this study. We further examined the correlations between ferroptosis, hub DE-FRGs, related pathways, and MRI-derived parameters, providing a potential biological basis for the identified imaging characteristics. The findings suggest that MRI-derived parameters may, to some extent, mirror the underlying pathophysiological alterations, laying a foundation for

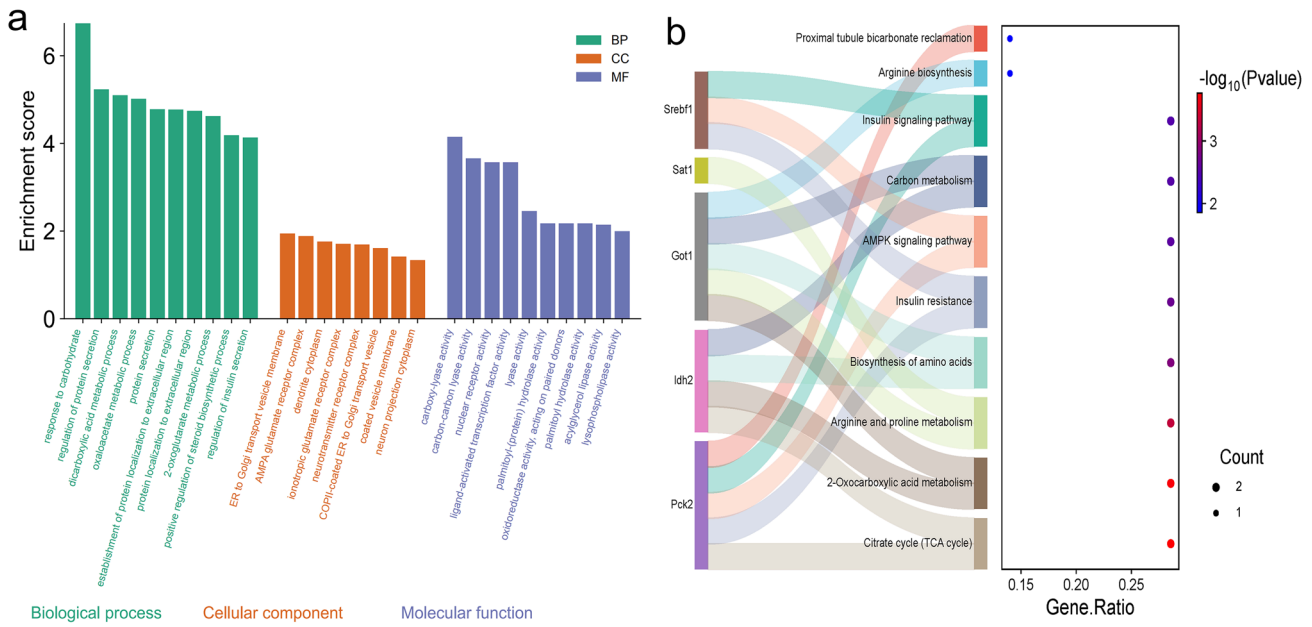

Fig. 7 Enrichment analysis of hub DE-FRGs in MASLD-related liver fibrosis. **a** Bar chart of GO enrichment analysis for hub DE-FRGs. **b** Sankey bubble chart of KEGG pathway enrichment for hub DE-FRGs

future investigations into radiogenomic interactions and their clinical translational potential.

Fads1 is the rate-limiting enzyme in the desaturation of polyunsaturated fatty acids (PUFAs), and its expression level is closely associated with PUFA content. PUFAs help reduce hepatic lipid accumulation [17]. Previous studies have shown that up-regulation of *Fads1* exerts hepatoprotective effects and reduces lipid accumulation [18], which is consistent with the findings of this study. It has also been reported that the PUFA biosynthesis pathway can influence fatty acid metabolism by regulating fatty acid uptake and β-oxidation, thereby participating in the regulation of ferroptosis [19]. However, whether *Fads1* mediates ferroptosis in MASLD through the PUFA synthesis pathway remains unclear and warrants further investigation. *Got1* is a pyridoxal-phosphate (PLP)-dependent aminotransferase and a key enzyme in amino acid metabolism, especially glutamine metabolism, it serves as an important bridge linking cellular metabolism and the tumor immune microenvironment [20, 21]. It affects cellular functions in multiple ways by regulating amino acid metabolism, energy metabolism, and redox balance [22]. In this study, enrichment analysis revealed that *Got1* is significantly enriched in amino acid biosynthesis, and its high expression in healthy liver tissue is consistent with its role in maintaining basic liver metabolism. Studies have shown that knockdown of *Got1* can cause mitochondrial dysfunction, leading to excessive ROS production, which in turn inhibits cell proliferation, promotes apoptosis, and increases susceptibility to ferroptosis [23, 24]. Notably, our TEM analysis revealed obvious mitochondrial abnormalities in fibrosis livers, including mitochondrial swelling and a significant decrease in cristae density, these ultrastructural changes are typical manifestations of mitochondrial damage and impaired oxidative metabolism. Therefore, the downregulation of *Got1* in the fibrosis group may be the result of hepatocyte metabolic dysfunction and mitochondrial damage. *Srebf1*, a core member of the bHLH-Zip transcription factor family, governs the synthesis and uptake of fatty acids and cholesterol [25]. Aberrant activity of *Srebf1* is linked to hepatic steatosis and to the metabolic reprogramming and poor prognosis observed in multiple cancers [26, 27]. A recent study confirmed that DDX39B can activate *Srebf1*, promoting lipid synthesis and malignant progression in HCC [28]. These findings support the results of the present study. *Abhd12* is a serine hydrolase of the α/β-hydrolase fold protein family whose core functions center on lipid metabolism and signal transduction. This gene has been reported to modulate tumor cells by interfering with lipid metabolism and the endocannabinoid signaling pathway [29]. Additionally, its aberrant expression may be associated with hepatic dysfunction [30], and this gene was up-regulated in our liver fibrosis cohort. *Idh2*, a key enzyme in the tricarboxylic acid cycle, catalyzes the reaction that directly generates α-ketoglutarate and NADPH [31]. Studies have reported that *Idh2* is down-regulated in HCC [32]. Pan et al. found that its deletion renders female mice more susceptible to fructose-induced MASLD and associated inflammation [33]. However, another study has shown that elevated hepatic *Idh2* levels promote gluconeogenesis and glycogenesis, suggesting that inhibiting liver

Table 2 Representative results of the hub DE-FRGs enrichment analysis

ID	Description	GeneRatio	BgRatio	pvalue	*p*.adjust	geneID	Count	Class
GO:0009743	response to carbohydrate	5/8	365/17,859	1.85E-07	7.80E-05	Pck2/Nr1d1/Fads1/Got1/Srebf1	5	BP
GO:0050708	regulation of protein secretion	4/8	310/17,859	5.90E-06	1.02E-03	Pck2/Idh2/Nr1d1/Srebf1	4	BP
GO:0043648	dicarboxylic acid metabolic process	3/8	95/17,859	8.01E-06	1.02E-03	Pck2/Idh2/Got1	3	BP
GO:0006107	oxaloacetate metabolic process	2/8	11/17,859	9.64E-06	1.02E-03	Pck2/Got1	2	BP
GO:0009306	protein secretion	4/8	403/17,859	1.66E-05	1.09E-03	Pck2/Idh2/Nr1d1/Srebf1	4	BP
GO:0035592	establishment of protein localization to extracellular region	4/8	405/17,859	1.70E-05	1.09E-03	Pck2/Idh2/Nr1d1/Srebf1	4	BP
GO:0071692	protein localization to extracellular region	4/8	412/17,859	1.82E-05	1.09E-03	Pck2/Idh2/Nr1d1/Srebf1	4	BP
GO:0006103	2-oxoglutarate metabolic process	2/8	17/17,859	2.38E-05	1.26E-03	Idh2/Got1	2	BP
GO:0010893	positive regulation of steroid biosynthetic process	2/8	28/17,859	6.60E-05	2.89E-03	Nr1d1/Srebf1	2	BP
GO:0050796	regulation of insulin secretion	3/8	199/17,859	7.32E-05	2.89E-03	Pck2/Nr1d1/Srebf1	3	BP
GO:0012507	ER to Golgi transport vesicle membrane	1/8	26/18,211	1.14E-02	1.19E-01	Srebf1	1	CC
GO:0032281	AMPA glutamate receptor complex	1/8	30/18,211	1.31E-02	1.19E-01	Abhd12	1	CC
GO:0032839	dendrite cytoplasm	1/8	40/18,211	1.74E-02	1.19E-01	Abhd12	1	CC
GO:0008328	ionotropic glutamate receptor complex	1/8	45/18,211	1.96E-02	1.19E-01	Abhd12	1	CC
GO:0098878	neurotransmitter receptor complex	1/8	47/18,211	2.05E-02	1.19E-01	Abhd12	1	CC
GO:0030134	COPII-coated ER to Golgi transport vesicle	1/8	57/18,211	2.48E-02	1.20E-01	Srebf1	1	CC
GO:0030662	coated vesicle membrane	1/8	89/18,211	3.84E-02	1.59E-01	Srebf1	1	CC
GO:0120111	neuron projection cytoplasm	1/8	108/18,211	4.65E-02	1.62E-01	Abhd12	1	CC
GO:0016831	carboxy-lyase activity	2/8	27/16,532	7.15E-05	2.82E-03	Pck2/Got1	2	MF
GO:0016830	carbon-carbon lyase activity	2/8	47/16,532	2.19E-04	2.82E-03	Pck2/Got1	2	MF
GO:0004879	nuclear receptor activity	2/8	52/16,532	2.68E-04	2.82E-03	Nr1d1/Srebf1	2	MF
GO:0098531	ligand-activated transcription factor activity	2/8	52/16,532	2.68E-04	2.82E-03	Nr1d1/Srebf1	2	MF
GO:0016829	lyase activity	2/8	190/16,532	3.52E-03	2.95E-02	Pck2/Got1	2	MF
GO:0008474	palmitoyl-(protein) hydrolase activity	1/8	14/16,532	6.76E-03	3.38E-02	Abhd12	1	MF
GO:0016717	oxidoreductase activity	1/8	14/16,532	6.76E-03	3.38E-02	Fads1	1	MF
GO:0098599	palmitoyl hydrolase activity	1/8	14/16,532	6.76E-03	3.38E-02	Abhd12	1	MF
GO:0047372	acylglycerol lipase activity	1/8	15/16,532	7.24E-03	3.38E-02	Abhd12	1	MF
GO:0004622	lysophospholipase activity	1/8	21/16,532	1.01E-02	4.25E-02	Abhd12	1	MF

Table 2 (continued)

ID	Description	GeneRatio	BgRatio	pvalue	*p*.adjust	geneID	Count	Class
rno00020	Citrate cycle (TCA cycle)	2/7	32/10,968	1.72E-04	2.91E-03	Pck2/Idh2	2	KEGG
rno01210	2-Oxocarboxylic acid metabolism	2/7	34/10,968	1.94E-04	2.91E-03	Idh2/Got1	2	KEGG
rno00330	Arginine and proline metabolism	2/7	55/10,968	5.10E-04	5.10E-03	Sat1/Got1	2	KEGG
rno01230	Biosynthesis of amino acids	2/7	93/10,968	1.45E-03	1.09E-02	Idh2/Got1	2	KEGG
rno04931	Insulin resistance	2/7	112/10,968	2.10E-03	1.19E-02	Pck2/Srebf1	2	KEGG
rno04152	AMPK signaling pathway	2/7	129/10,968	2.77E-03	1.19E-02	Pck2/Srebf1	2	KEGG
rno01200	Carbon metabolism	2/7	135/10,968	3.03E-03	1.19E-02	Idh2/Got1	2	KEGG
rno04910	Insulin signaling pathway	2/7	138/10,968	3.17E-03	1.19E-02	Pck2/Srebf1	2	KEGG
rno00220	Arginine biosynthesis	1/7	21/10,968	1.33E-02	4.19E-02	Got1	1	KEGG
rno04964	Proximal tubule bicarbonate reclamation	1/7	22/10,968	1.40E-02	4.19E-02	Pck2	1	KEGG

Idh2 could be a potential therapeutic target for obesity and diabetes [34], whereas, the present study observed up-regulation of *Idh2* in the liver fibrosis group. This discrepancy may indicate that *Idh2* plays distinct roles at different stages of liver disease. *Pck2*, *Nr1d1* and *Sat1* have not been extensively studied. In our study, *Nr1d1* was down-regulation in the liver-fibrosis group, whereas *Pck2* and *Sat1* were up-regulated in the liver-fibrosis group. These observations may provide new insights for elucidating the molecular mechanisms of hepatic fibrosis and identifying therapeutic targets. All of these genes are ferroptosis-related genes, and ferroptosis may play an important role in the pathogenesis of MASLD-related liver fibrosis, influencing disease progression. However, its precise function requires further experimental validation.

Enrichment analysis of the eight hub DE-FRGs indicated their potential involvement in BP, MF, and KEGG pathways, particularly those related to carbohydrate response, amino acid biosynthesis, insulin resistance, and AMPK signaling pathways. In recent years, research on MASLD has focused primarily on the roles of dietary carbohydrates and fats, while protein intake has received comparatively little attention. As the central organ for amino acid metabolism, the liver also serves as the primary site for the regulation of glucose and fatty acid partitioning [35]. Dietary glucose is mainly converted to glycogen for storage in the liver, whereas lactate produced by extrahepatic tissues enters the circulation, is taken up by the liver, and oxidized in the TCA cycle. Simultaneously, amino acids also accumulate extensively in the liver [36]. Dietary amino acids are markedly more efficient than glucose at promoting hepatic de novo lipogenesis, and their conversion to fatty acids via reductive carboxylation is further intensified in obesity [37]. Insulin resistance promotes the synthesis and accumulation of fatty acids and triglycerides in the liver, thereby exacerbating inflammatory responses and oxidative stress [38]. AMP-activated protein kinase (AMPK), a master regulator of energy metabolism, plays a pivotal role in glucose and fatty-acid homeostasis. Its activation suppresses the proliferation, activation, and migration of hepatic stellate cells and induces their apoptosis, thereby contributing to anti-fibrosis control [39]. In vivo studies further demonstrated that AMPK activation in CCl_4-induced liver fibrosis models effectively suppresses hepatic stellate cell proliferation, reduces α-SMA levels, and thereby ameliorates fibrosis lesions [40]. Taken together, our findings and previous reports indicate that these pathways play pivotal roles in fibrosis progression. Although they highlight potential therapeutic targets, their underlying mechanisms and translational relevance urgently await further investigation.

In the field of noninvasive diagnosis, MRI, owing to its high accuracy and sensitivity, can effectively distinguish simple hepatic steatosis from nonalcoholic steatohepatitis and precisely evaluate the degree of hepatic steatosis and fibrosis [41]. Multiple derived parameters have shown great potential for noninvasively assessing MASLD-related liver fibrosis. T2* is closely related to hepatic steatosis [42]. PDFF can estimate hepatic fat content, the increase of which is directly linked to fibrosis progression in MASLD [43]. R2* serves as a reliable noninvasive index for assessing hepatic iron content and systemic iron homeostasis, and in MASLD its elevation usually indicates hepatic iron overload [44]. Our results indicate that PDFF is closely linked to each of the hub DE-FRGs. Specifically, it shows negative correlations with *Fads1*, *Got1*, and *Nr1d1*, which are down-regulated in the fibrosis group, and positive correlations

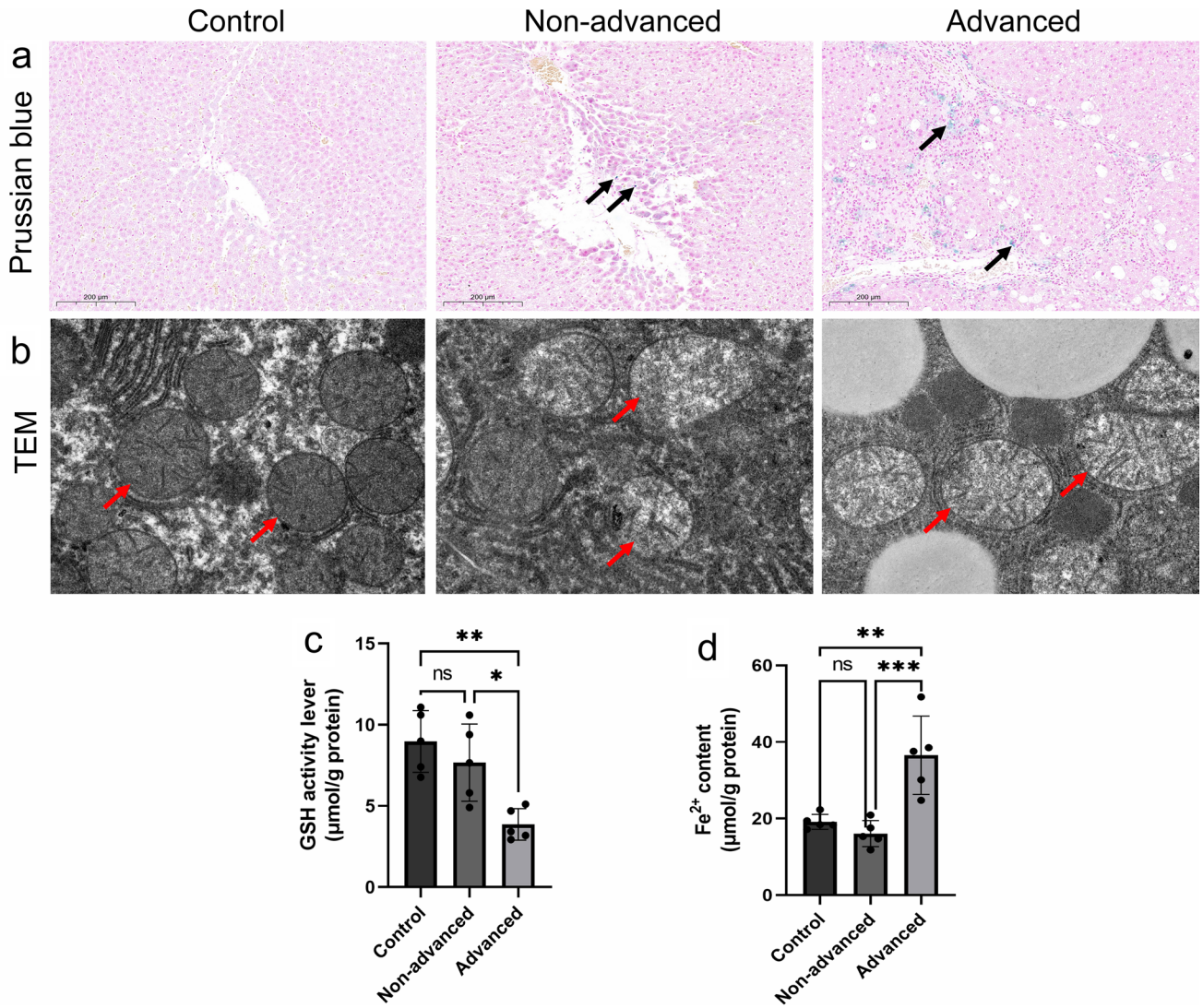

Fig. 8 Indirect indicators related to ferroptosis in rat models. **a** Prussian-blue staining, black arrow indicates the deposition of blue iron ions. **b** Transmission-electron-microscopy images, red arrow indicates the mitochondria. **c** GSH activity levels (5 samples per group). **d** Fe^{2+} content (5 samples per group). Results are presented as mean ± standard deviation (SD), statistical analysis was performed using one-way ANOVA. ns, indicates the difference is not statistically significant, * $p<0.05$, ** $p<0.01$, *** $p<0.001$

with *Abhd12*, *Idh2*, *Pck2*, *Sat1*, and *Srebf1*, which are up-regulated in the fibrosis group. These hub DE-FRGs are mainly associated with pathways related to carbohydrate response, amino acid biosynthesis, insulin resistance, and AMPK signaling. Consistent with previous research findings [44], our results show that R2* is positively correlated with Fe^{2+}, while T2* is negatively correlated with Fe^{2+}, further indicating that ferroptosis is closely associated with MASLD-related liver fibrosis. In summary, this study found that MRI-derived parameters not only reflect the macroscopic pathological changes of liver fibrosis, but also appear to be potentially associated with the process of ferroptosis, hub DE-FRGs, and related signaling pathways. This provides a novel window into the microscopic mechanisms underlying disease progression and highlights the expanding prospects of MRI for non-invasive assessment of liver fibrosis. However, these associations need to be further experimental confirmation.

However, this study has several limitations. First, although bioinformatics workflows effectively narrow down the range of potential ferroptosis-related targets, the variability among individual animals, differences in in vivo mRNA stability, and a small sample size may have prevented significant differences from being observed in the validation of certain genes, which could limit the generalizability of the research findings. Therefore, future validation of these targets would require larger sample sizes of both rats and humans, as well as additional experiments, such

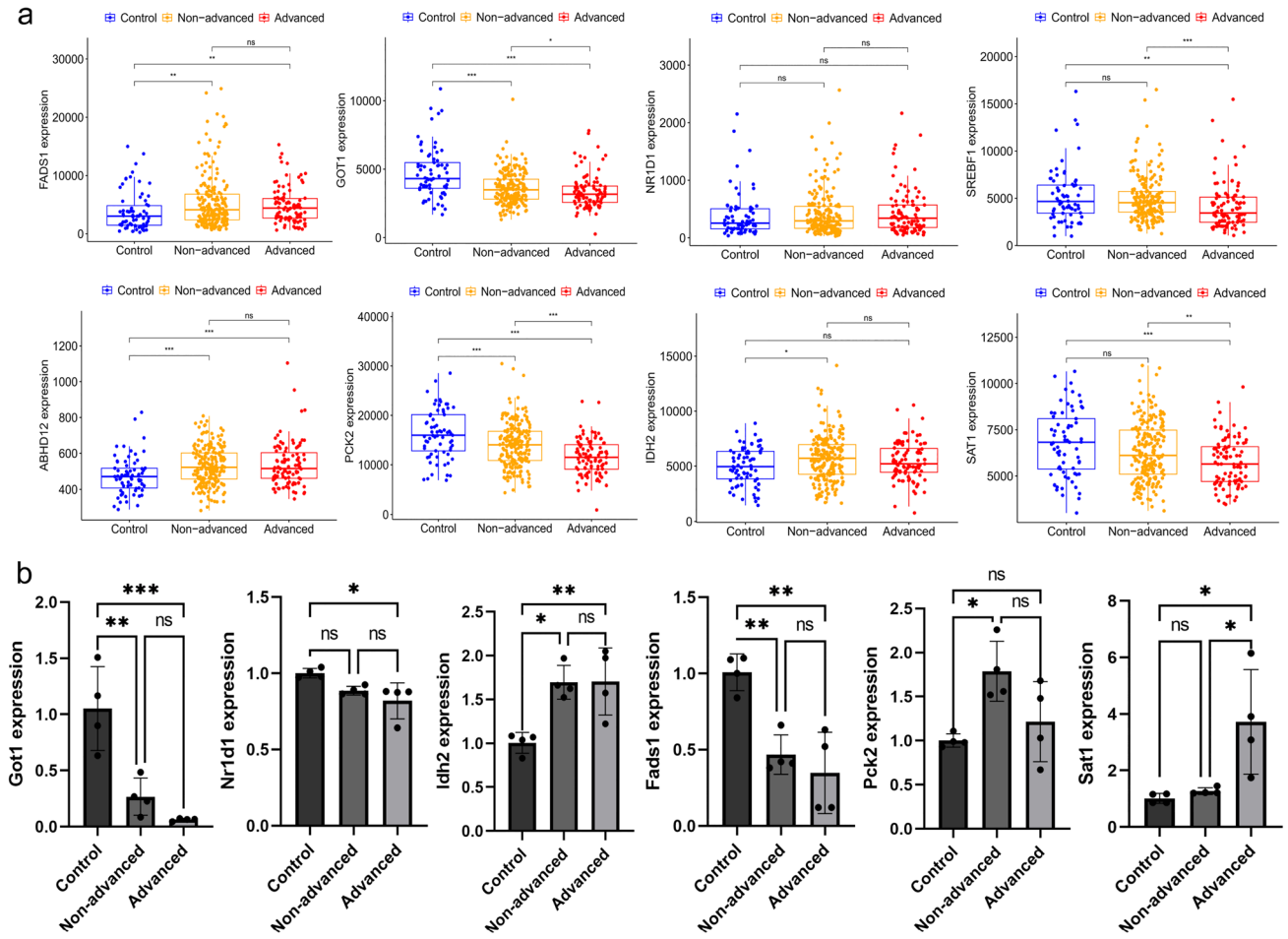

Fig. 9 Hub DE-FRGs validation results. **a** Expression of hub DE-FRGs in the public database GSE213621. **b** Expression of hub DE-FRGs in qRT-PCR experiments (4 samples per group). Results are presented as mean ± standard deviation (SD), statistical analysis was performed using one-way ANOVA. ns, indicates the difference is not statistically significant, * $p<0.05$, ** $p<0.01$, *** $p<0.001$

as immunohistochemical analysis or functional assays, to enhance statistical power and the reliability of the results. Second, the core results of this study are derived from a rat model, which may not fully replicate the progression of fibrosis observed in human MASLD. External validation data come from human samples, genetic and regulatory differences between species may affect the direct comparability of gene expression patterns. The inherent heterogeneity of public datasets, such as differences in patient clinical characteristics and sample handling, may introduce potential dataset bias. Future validation in more standardized, prospective clinical cohorts is needed to further confirm the translational potential of these biomarkers. In addition, although we have preliminarily identified and validated hub DE-FRGs and signaling pathways associated with MASLD-related liver fibrosis, their exact biological functions remain unclear and require further validation through in vitro experiments. Finally, this study did not assess lipid peroxidation biomarkers related to ferroptosis. Although we observed ultrastructural changes as well as increases in Fe^{2+} and decreases in GSH, these changes are not unique to ferroptosis and cannot be used alone as definitive evidence of its occurrence. The conclusions of this study regarding ferroptosis are still mainly based on indirect evidence, and therefore can only suggest that ferroptosis is related to the development of MASLD-related liver fibrosis. Future work needs to directly measure lipid peroxides and conduct functional experiments to further validate.

Conclusion

By establishing an animal model and integrating transcriptome sequencing with bioinformatics analysis, this study successfully identified eight hub DE-FRGs related to MASLD fibrosis and elucidated the key signaling pathways in which they are involved. Furthermore, the integration of multiparametric MRI revealed associations between MRI-derived parameters and ferroptosis, as well as the aforementioned hub DE-FRGs and pathways, indicating that MRI

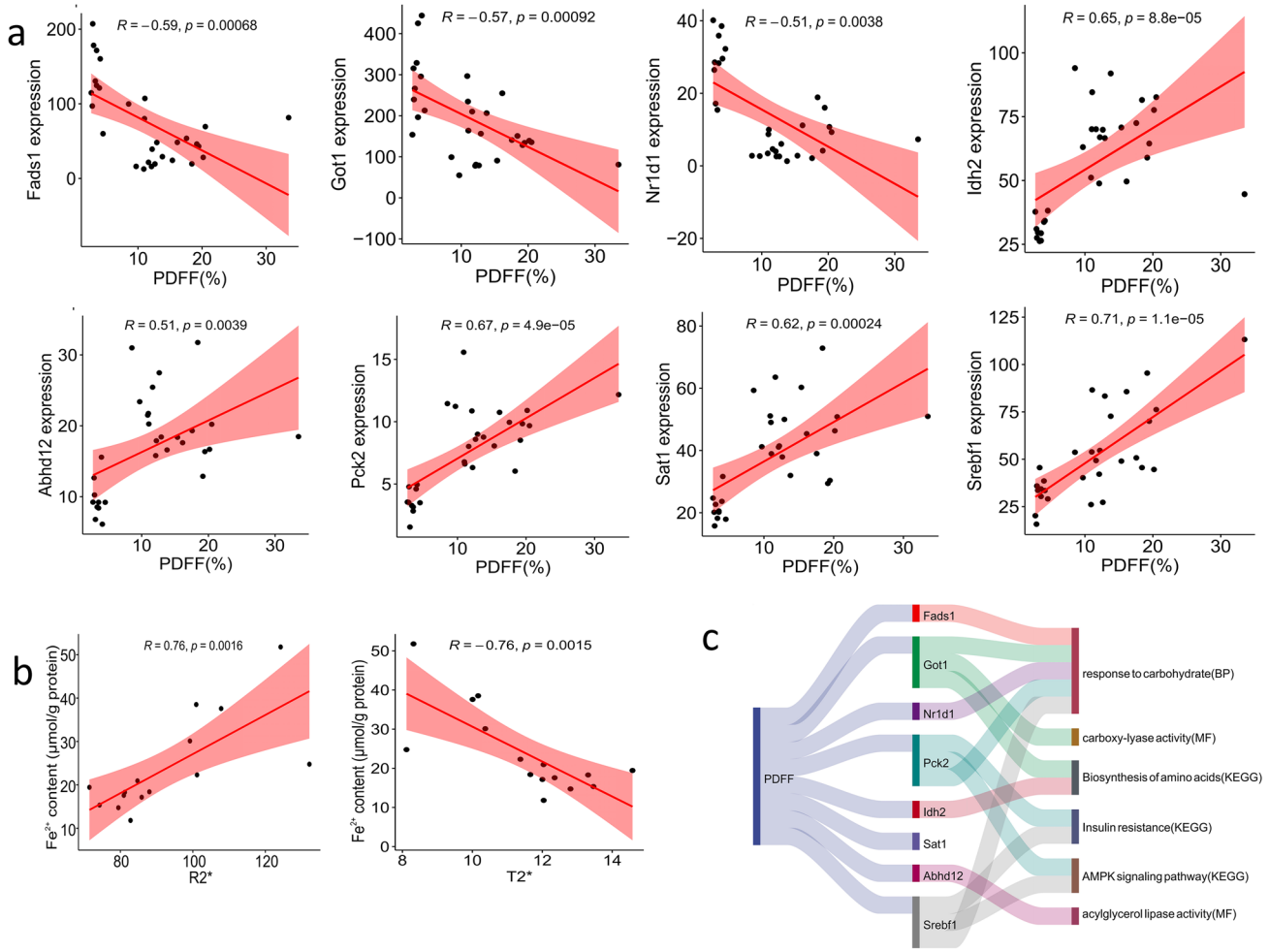

Fig. 10 Correlation analysis results. **a** Scatter plots illustrating the correlations between hub DE-FRGs and PDFF. **b** Scatter plots illustrating the correlations of Fe^{2+} content with R2*and T2*. **c** Sankey diagram illustrating the associations among PDFF, hub DE-FRGs, and their representative biological functions

technology holds significant potential for the noninvasive evaluation of hepatic fibrosis. These findings deepen our understanding of MASLD-related liver fibrosis. However, this study represents only a preliminary exploration, and further experiments and data will be required to confirm and expand upon these observations.

Supplementary Information The online version contains supplementary material available at https://doi.org/10.1007/s10238-025-02034-x.

Acknowledgements We thank all of StudyForBetter team members for their collaboration.

Author contributions All authors contributed to the study conception and design. YMH was responsible for data organization, research investigation, and drafting the initial manuscript; XQ, LFY, CC, and WTY were responsible for experimental validation, TMW, and YMH primarily in charge of conceptual construction and formal analysis; HJ, PY and DR handled methodology and statistical analysis, LPG and LP oversaw project management, resources, supervision, and funding acquisition. All authors read and approved the final manuscript.

Funding This study was partially supported by the Excellent Reserve Talents Funding within the Discipline at the Affiliated Hospital of Guizhou Medical University (gyfyxkyc−2023−13), the Guizhou Provincial Science and Technology Projects (Qiankehejichu-ZK[2023]353), the National Natural Science Foundation of China Cultivation Project facilitated by the Affiliated Hospital of Guizhou Medical University (gyfynsfc[2023]−03), the Guizhou Province High-level Innovative Talent Program (gzwjrs 2023−019), and the National Key Research and Development Program (Grant No. 2022YFC2503003).

Data availability The datasets analyzed during the current study are available in the following repositories: The NCBI GEO database (https://www.ncbi.nlm.nih.gov/geo/).The FerrDbv2 database (http://www.zhounan.org/ferrdb/current/).Additional data are available from the corresponding author upon request.

Declarations

Competing interests The authors declare no competing interests.

Ethical approval All research procedures involving animals comply

with the ethical standards of the Ethics Committee of Guizhou Medical University.

Consent to participate Not applicable.

Consent to publish Not applicable.

References

1. Diehl Anna M, Christopher D. Cause, pathogenesis, and treatment of nonalcoholic steatohepatitis. N Engl J Med. 2017;377:2063–72.
2. Friedman SL, Neuschwander-Tetri BA, Rinella M, Sanyal AJ. Mechanisms of NAFLD development and therapeutic strategies. Nat Med. 2018;24:908–22.
3. Younossi ZM, Golabi P, Paik JM, Henry A, Van Dongen C, Henry L. The global epidemiology of nonalcoholic fatty liver disease (NAFLD) and nonalcoholic steatohepatitis (NASH): a systematic review. Hepatology. 2023;77:1335–47.
4. Paik JM, Henry L, Younossi Y, Ong J, Alqahtani S, Younossi ZM. The burden of nonalcoholic fatty liver disease (NAFLD) is rapidly growing in every region of the world from 1990 to 2019. Hepatol Commun. 2023;7:e0251.
5. Heyens L, Busschots D, Koek GH, Robaeys G, Francque S. Liver fibrosis in non-alcoholic fatty liver disease: from liver biopsy to non-invasive biomarkers in diagnosis and treatment. Front Med Lausanne. 2021;8:615978.
6. Powell EE, Wong VW, Rinella M. Non-alcoholic fatty liver disease. Lancet. 2021;397:2212–24.
7. Fang Z, Liu C, Cheng Y, Ji Y, Liu C. Combined analysis of bulk, single-cell RNA sequencing, and spatial transcriptomics reveals the expression patterns of lipid metabolism and ferroptosis in the immune microenvironment of metabolic-associated fatty liver disease. Life Sci. 2025;362:123377.
8. Dixon SJ, Lemberg KM, Lamprecht MR, et al. Ferroptosis: an Iron-Dependent form of nonapoptotic cell death. Cell. 2012;149:1060–72.
9. Naoya Y, Tadayoshi K, Hiroaki K, et al. Ferroptosis driven by radical oxidation of n–6 polyunsaturated fatty acids mediates acetaminophen-induced acute liver failure. Cell Death Dis. 2020;11:144.
10. Tsurusaki S, Tsuchiya Y, Koumura T, et al. Hepatic ferroptosis plays an important role as the trigger for initiating inflammation in nonalcoholic steatohepatitis. Cell Death Dis. 2019;10:449.
11. Lei P, Hu N, Wu Y, et al. Radiobioinformatics: a novel bridge between basic research and clinical practice for clinical decision support in diffuse liver diseases. iRadiology. 2023;1:167–89.
12. Hartmann K, Sadée CY, Satwah I, Carrillo-Perez F, Gevaert O. Imaging genomics: data fusion in uncovering disease heritability. Trends Mol Med. 2023;29:141–51.
13. Segal E, Sirlin CB, Ooi C, et al. Decoding global gene expression programs in liver cancer by noninvasive imaging. Nat Biotechnol. 2007;25:675–80.
14. Selvaraj EA, Mózes FE, Jayaswal A, et al. Diagnostic accuracy of elastography and magnetic resonance imaging in patients with NAFLD: A systematic review and meta-analysis. J Hepatol. 2021;75:770–85.
15. Huang Z, Xia X, Liang Y, et al. Assessment and integration of multiparametric MRI for liver fibrosis staging in rat non-alcoholic steatohepatitis: evaluation of diagnostic efficiency and model interpretation. Eur J Radiol. 2025;182:111821.
16. Kang JW, Hong JM, Lee SM. Melatonin enhances mitophagy and mitochondrial biogenesis in rats with carbon tetrachloride-induced liver fibrosis. J Pineal Res. 2016;60:383–93.
17. Martinelli N, Girelli D, Malerba G, et al. FADS genotypes and desaturase activity estimated by the ratio of arachidonic acid to linoleic acid are associated with inflammation and coronary artery disease. Am J Clin Nutr. 2008;88:941–9.
18. Athinarayanan S, Fan YY, Wang X, et al. Fatty acid desaturase 1 influences hepatic lipid homeostasis by modulating the PPARα-FGF21 axis. Hepatol Commun. 2021;5:461–77.
19. Kim JW, Lee JY, Oh M, Lee EW. An integrated view of lipid metabolism in ferroptosis revisited via lipidomic analysis. Exp Mol Med. 2023;55:1620–31.
20. Abrego J, Gunda V, Vernucci E, et al. GOT1-mediated anaplerotic glutamine metabolism regulates chronic acidosis stress in pancreatic cancer cells. Cancer Lett. 2017;400:37–46.
21. Zhou X, Curbo S, Li F, Krishnan S, Karlsson A. Inhibition of glutamate oxaloacetate transaminase 1 in cancer cell lines results in altered metabolism with increased dependency of glucose. BMC Cancer. 2018;18:559.
22. Xu W, Patel CH, Zhao L, et al. GOT1 regulates CD8(+) effector and memory T cell generation. Cell Rep. 2023;42:111987.
23. Liu Z, Han B, Liu K, et al. Multi-omics revealed GOT1/ALDH3A1 pathway attenuated head and neck squamous cell carcinoma and increased cisplatin sensitivity through ROS induced by mitochondrial dysfunction. Redox Rep. 2025;30:2588031.
24. Kremer DM, Nelson BS, Lin L, et al. GOT1 inhibition promotes pancreatic cancer cell death by ferroptosis. Nat Commun. 2021;12:4860.
25. Cheng C, Geng F, Cheng X, Guo D. Lipid metabolism reprogramming and its potential targets in cancer. Cancer Commun. 2018;38:27.
26. Zhao Q, Lin X, Wang G. Targeting SREBP−1-mediated lipogenesis as potential strategies for cancer. Front Oncol. 2022;12:952371.
27. Li C, Peng X, Lv J, et al. SREBP1 as a potential biomarker predicts levothyroxine efficacy of differentiated thyroid cancer. Biomed Pharmacother. 2020;123:109791.
28. Feng T, Li S, Zhao G, et al. DDX39B facilitates the malignant progression of hepatocellular carcinoma via activation of SREBP1-mediated de novo lipid synthesis. Cell Oncol (Dordr). 2023;46:1235–52.
29. Jun S, Kim SW, Lim JY, Park SJ. ABHD12 knockdown suppresses breast cancer cell proliferation, migration and invasion. Anticancer Res. 2020;40:2601–11.
30. Chambers JC, Zhang W, Sehmi J, et al. Genome-wide association study identifies loci influencing concentrations of liver enzymes in plasma. Nat Genet. 2011;43:1131–8.
31. Bergaggio E, Piva R. Wild-type IDH enzymes as actionable targets for cancer therapy. Cancers (Basel). 2019;11:563.
32. Liu WR, Tian MX, Jin L, et al. High expression of 5-hydroxymethylcytosine and isocitrate dehydrogenase 2 is associated with

favorable prognosis after curative resection of hepatocellular carcinoma. J Exp Clin Cancer Res. 2014;33:32.
33. Pan JH, Kim HS, Beane KE, et al. IDH2 deficiency aggravates fructose-induced NAFLD by modulating hepatic fatty acid metabolism and activating inflammatory signaling in female mice. Nutrients. 2018;10:679.
34. Wang H, Xiong Q, He G, et al. Hepatic IDH2 regulates glycolysis and gluconeogenesis. Metabolism. 2023;143:155559.
35. Coen CP, Wouter HL, Stefan B, Stan FJvdG. Amino acid metabolism, transport and signalling in the liver revisited. Biochem Pharmacol. 2022;201:115074.
36. Wang Z, Ying Z, Bosy-Westphal A, et al. Specific metabolic rates of major organs and tissues across adulthood: evaluation by mechanistic model of resting energy expenditure. Am J Clin Nutr. 2010;92:1369–77.
37. Liao Y, Chen Q, Liu L, et al. Amino acid is a major carbon source for hepatic lipogenesis. Cell Metab. 2024;36:2437–e488.
38. Palma R, Pronio A, Romeo M, et al. The role of insulin resistance in fueling NAFLD pathogenesis: from molecular mechanisms to clinical implications. J Clin Med. 2022;11:3649.
39. Currais A. Ageing and inflammation - a central role for mitochondria in brain health and disease. Ageing Res Rev. 2015;21:30–42.
40. Kumar P, Smith T, Rahman K, Thorn NE, Anania FA. Adiponectin agonist ADP355 attenuates CCl4-induced liver fibrosis in mice. PLoS One. 2014;9:e110405.
41. Troelstra MA, Witjes JJ, van Dijk AM, et al. Assessment of imaging modalities against liver biopsy in nonalcoholic fatty liver disease: the Amsterdam NAFLD-NASH cohort. J Magn Reson Imaging. 2021;54:1937–49.
42. Obmann VC, Marx C, Berzigotti A, et al. Liver MRI susceptibility-weighted imaging (SWI) compared to T2* mapping in the presence of steatosis and fibrosis. Eur J Radiol. 2019;118:66–74.
43. Ajmera V, Park CC, Caussy C, et al. Magnetic resonance imaging proton density fat fraction associates with progression of fibrosis in patients with nonalcoholic fatty liver disease. Gastroenterology. 2018;155:307–e102.
44. Xia H, Min Y, Wang Y, et al. Multiparametric MRI evaluation of liver fat and iron after glucagon-like peptide−1 receptor and glucagon receptor dual-agonist treatment in a high-fat diet-induced mouse model. Radiology. 2025;316:e243780.

Authors and Affiliations

Meihua Yang[1] · Qian Xu[1] · Fangyan Li[2] · Chen Chen[1] · Tianyuan Wang[1] · Maowen Tang[2] · Menghua Yang[2] · Jian He[2] · Yue Pan[2] · Rao Dai[2] · Pinggui Lei[1,2] · Peng Luo[1,3]

✉ Pinggui Lei
pingguilei@foxmail.com

✉ Peng Luo
luopeng@gmc.edu.cn

Meihua Yang
1494211905@qq.com

Qian Xu
2844145356@qq.com

Fangyan Li
1272181625@qq.com

Chen Chen
3328309562@qq.com

Tianyuan Wang
1659574416@qq.com

Maowen Tang
718233983@qq.com

Menghua Yang
18325166953@163.com

Jian He
2338434816@qq.com

Yue Pan
yuepan_79@163.com

Rao Dai
1502858012@qq.com

[1] School of Public Health, Guizhou Medical University, Guiyang of Guizhou 550004, China

[2] Department of Radiology, The Affiliated Hospital of Guizhou Medical University, Guiyang of Guizhou 550004, China

[3] The Key Laboratory of Environmental Pollution Monitoring and Disease Control, Ministry of Education, Guizhou Medical University, Guiyang of Guizhou 550004, China